Open Ceramics 20 (2024) 100696

Contents lists available at ScienceDirect

Open Ceramics

journal homepage: www.sciencedirect.com/journal/open-ceramics

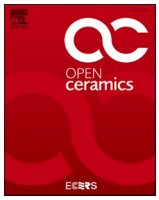

# Thermal properties of $MB_2$-WC (M = Ti, Zr, Hf) and tungsten and their stability after deuterium plasma exposure

Pietro Galizia [a,*], Andrea Uccello [b], Francesco Ghezzi [b], Luca Labate [c], Bruno Tiribilli [d], Ondrej Hanzel [e], Martina Salvadori [c], Fernando Brandi [c], Simone Failla [a], Cesare Melandri [a], Anna Cremona [b], Matteo Pedroni [b], Marco De Angeli [b], Enrico Perelli Cippo [b], Leonida Antonio Gizzi [c], Peter Tatarko [e], Diletta Sciti [a]

[a] CNR-ISSMC, National Research Council of Italy - Institute of Science, Technology and Sustainability for Ceramics, Via Granarolo 64, 48018, Faenza, Italy
[b] CNR-ISTP, National Research Council of Italy - Institute for Plasma Science and Technology, Via R. Cozzi 53, 20125, Milano, Italy
[c] CNR-INO, National Research Council of Italy - National Institute of Optics, Pisa, Via Moruzzi, 1, 56124 Pisa, Italy
[d] CNR-ISC, National Research Council of Italy - Institutes for Complex Systems, Via Madonna del Piano 10, 50019, Sesto Fiorentino, Italy
[e] IIC-SAS, Institute of Inorganic Chemistry, Slovak Academy of Sciences, Dúbravská cesta 9, 845 36, Bratislava, Slovakia

ARTICLE INFO

Handling Editor: P Colombo

*Keywords:*
Tungsten
Ultra-high temperature ceramic
Plasma-facing material
Deuterium ion irradiation
Thermal conductivity
Thermal effusivity

ABSTRACT

The thermal properties of ultra-high temperature ceramics (UHTCs) in the $MB_2$-WC (M = Ti, Zr, Hf) system and tungsten were studied for potential application as plasma-facing materials in fusion power plants. The sintered UHTC and tungsten samples were subjected to deuterium plasma or protons irradiation. Thermal diffusivity was measured using the laser flash method, and superficial thermal conductivity was analyzed through atomic force microscopy. Results showed that the thermal properties did not degrade when exposed to relevant environments and remained stable over a range of temperatures, unlike the reference tungsten material. Thermal conductivity ranged from 61 to 68 W $m^{-1}$ $K^{-1}$ for $TiB_2$-2(WC-6Co), from 53 to 63 W $m^{-1}$ $K^{-1}$ for $ZrB_2$-6WC, from 67 to 75 W $m^{-1}$ $K^{-1}$ for $HfB_2$-6WC, and from 180 to 119 W $m^{-1}$ $K^{-1}$ for tungsten across the temperature range from room temperature to 1200 °C. The increasing trend of thermal effusivity, over 19000 J $s^{-0.5}$ $m^{-2}$ $K^{-1}$ at 1200 °C, justifies further testing and of UHTC materials for fusion applications.

## 1. Introduction

Ultra-high temperature ceramics (UHTCs) have demonstrated remarkable resistance to extreme environments [1–4] and are attracting significant interest in strategic areas, such as aerospace [5–12] and energy [13–19]. Their potential to address the materials science challenges associated with the unique deuterium-tritium fusion environment expected in the ITER power plant is particularly notable [20]. Within the reactor vessel, the divertor faces challenges, such as intense heat flux of 5–20 MW/$m^2$, thermal shock exceeding 600 °C in less than a second, thermal gradient of 200 °C/mm, and exposure to hydrogen isotope ions, neutrons, gamma, and X-rays. Since the 1979 Miami Beach topical meeting on fusion materials [21], significant progress has been made in the development of Plasma Facing Materials (PFMs), with tungsten-based materials emerging as leading contenders for various reactor components. To date, a final decision on the use of PFMs in future fusion reactors remains pending [20,21]. Tungsten-based materials, for instance, present challenges related to structural integrity, including susceptibility to brittle failure [22], as demonstrated by Hong Zhang et al. in Ref. [23]. In this work, tungsten samples were exposed to a deuterium plasma on a linear plasma device with a fluence of 1.5e25 ions/$m^2$, a flux of 1e21 ions/$m^2$s, and an ion energy of 38 eV/ions (to avoid the creation of defects by displacement damage [24]), with temperature controlled at 127 °C and 450 °C. In this context, the study of

* Corresponding author.
*E-mail address:* pietro.galizia@cnr.it (P. Galizia).

https://doi.org/10.1016/j.oceram.2024.100696
Received 27 June 2024; Received in revised form 20 September 2024; Accepted 9 October 2024
Available online 10 October 2024

transition metal diborides ceramics, $MB_2$ (M = Ti or Zr) [14–18,25] becomes relevant. In fact, despite their brittle behaviour, as also observed in tungsten, these materials offer intrinsic thermal stability combined with high thermal conductivity ranging from 50 to 120 W $m^{-1}$ $K^{-1}$, even at temperatures up to 2000 °C [1–4,26–30]. Previous studies show $ZrB_2$, irradiated with 30 keV $He^+$ to fluences up to 5e22 He/$m^2$ at temperatures up to ~850 °C, displayed similar mass loss as tungsten [14]. $ZrB_2$, irradiated with 4 MeV $Au^{2+}$ at a fluence of 2.5e20 ions/$m^2$, exhibited substantial resilience to irradiation-induced damage, maintaining structural integrity with mild lattice damage down to a depth of 1150 nm [17]. $TiB_2$, when irradiated at 200 °C and 600 °C up to 2.4e25 neutrons/$m^2$ (E > 0.1 MeV) with a total dose of ~4.2 displacements per atom, was found to be susceptible to helium-induced cavity formation [15,16]. However, isotopic boron-11 enrichment minimizes helium generation and potentially prevents severe degradation in $MB_2$ ceramics [15,16]. These tests on $ZrB_2$ and $TiB_2$ highlight the potential of $MB_2$ ceramics for use as PFMs. Given their strong thermal properties, in this work, the thermal conductivity of group IV transition metal diboride $MB_2$-based ceramics (M = Ti, Zr or Hf) sintered with tungsten carbide was investigated both before and after exposure to deuterium plasma and protons irradiation. It is worth noting that sintering aids, such as Mo, Cr and Si based materials were avoided to reduce the activation potential. In addition, the amount of carbon was limited to avoid fuel retention [31,32], although carbon can improve thermal conductivity [33]. While the bulk ceramics may not be suitable for direct application as plasma-facing materials (PFMs) due to their limited thermal shock resistance, they show promise as coatings for the tiles of tokamak reactors [34] and/or as matrices in tougher composites [35–38]. These materials could provide a viable alternative to tungsten-based PFMs, advancing the quest for sustainable fusion energy.

In this paper, section 2 details the experimental methods, including the novel material preparation, plasma exposures, and thermal property measurements. The sintering behaviour and the microstructure of the developed $MB_2$-WC are presented for the first time in the initial part of section 3. Subsequently, section 3 discusses the results of the thermal properties and explores the implications of these findings for the use of $MB_2$-WC composites as potential PFMs. Finally, section 4 synthesizes the main findings and draws the conclusions.

## 2. Experimental

### 2.1. Material manufacturing

Commercial powders were used to prepare the ceramic materials. Table 1 shows some characteristics of the raw powders.

A conventional ceramic processing route was employed to produce $ZrB_2$ and $HfB_2$ with 6 mol% WC compositions. First, powder mixtures of $ZrB_2$ + 6 mol% WC (equivalent to 4.1 vol% and 10.0 wt%) and $HfB_2$ + 6 mol% WC (equivalent to 4.0 vol% and 5.9 wt%) were ball milled. In particular, 277.05 g of $ZrB_2$ plus 30.69 g of WC (labelled ZW6) and 239.48 g of $HfB_2$ plus 14.96 g of WC (labelled HW6) were milled for 72 h using 15 mm WC-6 wt.% Co spheres in a PE bottle of 1 L with a powder/spheres/ethanol weight ratio of 1/2.4/0.2. After drying via rotavapor at 85 °C, the powders were dry milled in the same previous bottles with the same milling media for 4 h in order to disaggregate the powders and make easier the following sieving at 250 μm.

For the $TiB_2$-WC composition, WC was added through a high energy milling with WC-6 wt% Co spheres, as reported in Ref. [39], to improve the densification thanks to the synergistic action of WC impurities, acting as sintering aid, and size reduction of the starting $TiB_2$ powders [40–43]. In particular, the starting $TiB_2$ powders were milled by high energy milling in a WC jar using 0.5 mm WC-6Co spheres, in air. The powder mixtures were then separated from the spheres, weighted, dried via rotavapor and sieved. The contamination of WC was expected to be around 2 mol% (equivalents to 1.6 vol% and 5.4 wt%) and for this reason the as produced $TiB_2$-WC composition was labelled TW2.

All powders were shaped in a disk of 45 mm of diameter under linear pressure of 60 bar. Then the disks were hot-pressed in the vacuum range of 0.1–1 mbar using an induction-heated graphite die, which allowed a heating rate above 1200 °C/h (the time required for the heating stage from 950 °C was about 25 min), and applying a constant uniaxial pressure of 35 MPa. The sintering temperatures and dwell times are detailed in Table 2. Dwell times were adjusted from 5 to 50 min to achieve a stable shrinkage plateau and a good densification. The change in thickness of the green pellets under hot-pressing was recorded during heating up and final dwell and then converted into relative density data, under the hypothesis of a full mass conservation. The temperature was monitored by means of an optical pyrometer focused into a blind hole dug on the external surface of the graphite die. At the end of the dwell, free cooling followed. The detail of heating rate and the calculated

**Table 1**
Details of the raw powders used.

| Formula | Company | Type | Density (g/cm$^3$) | Particle size, D | Maximum impurity (wt%) |
|---|---|---|---|---|---|
| $TiB_2$ | H.C. Starck | Grade F | 4.52 | $D_{90}$: 4.0–7.0 μm<br>$D_{50}$: 2.5–3.5 μm | 0.4 C, 2.5 O, 0.5 N, 0.1 Fe |
| $ZrB_2$ | H.C. Starck | Grade B | | Range: 0.5–6 μm | 0.2 C, 1.3 O, 0.19 N, 0.1 Fe, 1.4 Hf |
| $HfB_2$ | Cerac Incorporated | H-1002 | | −325 mesh | 0.07 Al, 0.01 Fe, 0.47 Zr (purity: 99.5 %) |
| WC | H.C. Starck | DS 60 | 15.63 | Fisher number: 0.60–0.70 μm | 2 Zr (purity: 99.5 %) |

**Table 2**
Starting composition, sintering process parameters (sintering onset temperature: $T_{ON}$; sintering temperature: T; dwell time: t), thickness of the disks (h), theoretical densities ($\rho_{th}$), experimental densities ($\rho$) and relative density ($p_{rel}$) of the green and sintered disks.

| Label | Starting composition | Green disk | | | | Sintering process | | | Sintered disk | | |
|---|---|---|---|---|---|---|---|---|---|---|---|
| | | $\rho_{th}$ | h | $\rho$ | $\rho_{rel}$ | $T_{ON}$ | T | t | h | $\rho$ | $\rho_{rel}$ |
| | (mol%) | (g/cm$^3$) | (mm) | (g/cm$^3$) | (%) | (°C) | (°C) | (min) | (mm) | (g/cm$^3$) | (%) |
| TW2 | $TiB_2$+2(WC-6Co) | 5.07 | 28.9 | 2.2 | 47 | 1010 | 1903 ± 8 | 5.1 | 13.2 | 4.55 ± 0.02 | 97 |
| ZW6 | $ZrB_2$+6WC | 6.47 | 29.6 | 3.2 | 49 | 1400 | 1931 ± 7 | 30.1 | 13.8 | 6.52 ± 0.02 | 99 |
| HW6 | $HfB_2$+6WC | 10.71 | 23.5 | 5.4 | 50 | 1700 | 1932 ± 4 | 47.7 | 10.3 | 11.16 ± 0.12 | 99 |

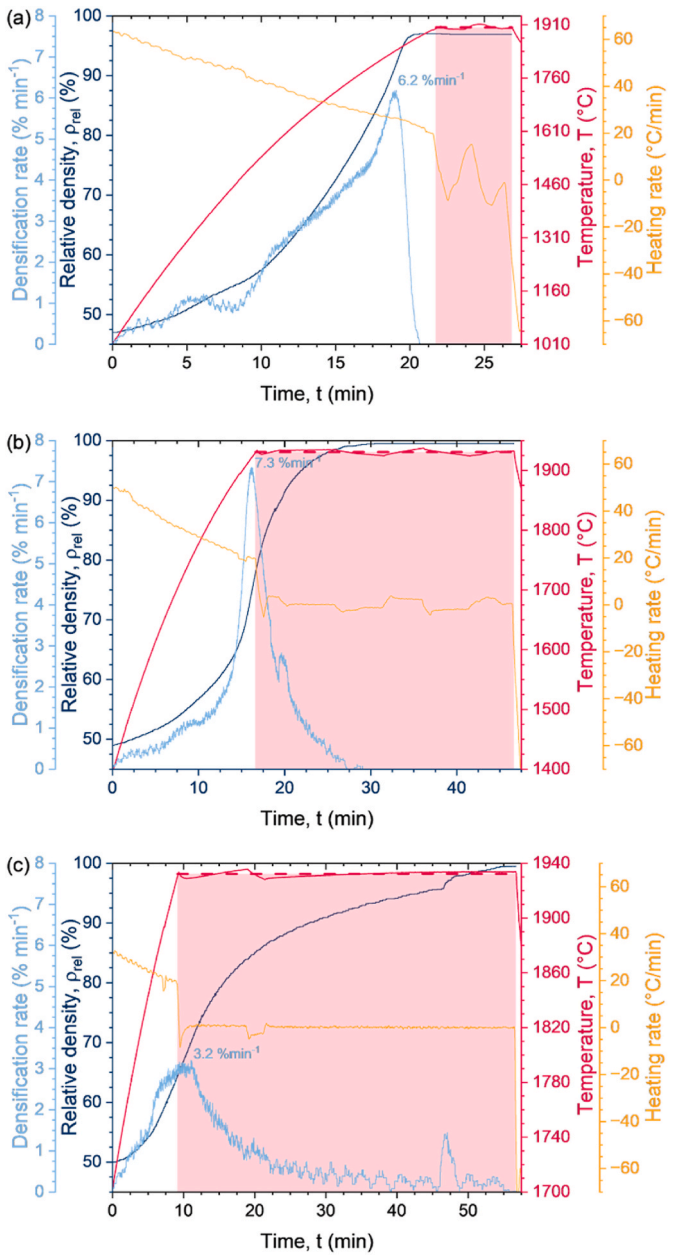


**Fig. 1.** Relative density (blue curve, left Y-axis) and densification rate (cyan curve, left Y-axis) vs. time (starting with sintering onset) for materials (a) TW2, (b) ZW6, and (c) HW6. The curves start from the onset temperature, set at time t = 0 min. The dashed red line, superimposed on the temperature curves, represents the average sintering temperature achieved during the dwell time (highlighted as the filled area under the curve). The temperature profile (red curve) and the corresponding heating rate (orange curve) are shown on the right Y-axis. (For interpretation of the references to colour in this figure legend, the reader is referred to the Web version of this article.)

continuous densification of the pellets are showed in Fig. 1.

From the sintered pellets 12.5 mm × 12.5 mm x 1 mm tiles were machined. A 12.5 mm × 12.5 mm surface of the tiles was manually polished using diamond paste from 30 μm down to 0.25 μm grain size.

### 2.2. Microstructural characterization

Final density was measured using the Archimedes' method in distillate water according to the ASTM C373-88 standard. The relative density was estimated as the ratio between the measured value and the theoretical value determined through the rule of mixtures on the basis of starting nominal compositions. The microstructural features were analyzed on fractured and polished sections of the sintered samples surfaces by scanning electron microscopy (FE-SEM, Carl Zeiss Sigma NTS Gmbh, Oberkochen, DE) and energy dispersive x-ray spectroscopy (EDS, INCA Energy 300, Oxford instruments, UK). Crystalline phases were identified by X-Ray Diffraction (XRD) at room temperature through a Bruker D8 Advance X-ray diffractometer (θ–θ) equipped with a LINXEYE detector (Bruker, Karlsruhe, Germany) using Cu Kα radiation (λ = 1.5418 Å) in the $10° \leq 2\theta \leq 150°$ range with a scanning step of 0.0105° and step time of 0.5 s.

The topological characterization of the surfaces was performed with a non-contact 3D profilometer (Taylor-Hobson CCI MP, Leicester, UK) equipped with a green light and a 20× magnification objective lens. An area of 6 × 6 $mm^2$ at the centre of each sample were scanned along two orthogonal directions and the collected surface data were processed with the Talymap 6.2 software (Taylor-Hobson, Leicester, UK). The evaluation of 2D texture parameters, through mean surface roughness ($R_a$), was performed on 4 different profiles extracted from the 3D data and a cut-off <0.8 mm and the gaussian filter for the separation of the roughness and waviness components were set according to the ISO 4288:2000. The 2D parameters were calculated as average of estimated values on all sampling lengths over each profile.

### 2.3. Exposure in relevant environments

To study the plasma interactions, the polished surface of sintered samples was subjected to deuterium plasma irradiation in the linear device GyM [44] at ion energies of 50 eV, 110 eV, 230 eV, 330 eV or 400 eV and a flux of 5e20 ions/($m^2$s), for 5 h, and 10 h, along with reference tungsten samples. For each irradiation condition, four samples (one tile for each material: TW2, ZW6, HW6 and reference W) were mounted in the sample holder as shown in Fig. 2, leaving an exposed surface of about 10 × 10 $mm^2$. The reference tungsten, supplied by FB Tecno S.r.l., was produced through powders pressing and sintering, followed by thermomechanical deformation. It was characterized by a purity ≥99.95 %, density of 19.3 g/$cm^3$, ultimate strength of 800 MPa, compressive strength of 1150 MPa, elastic modulus of 410 GPa, hardness HV30 of 460. The machined W samples had a roughness $R_a \leq 0.2$um. During the exposures in GyM, the temperature of the samples reached approximately at 200 °C at −22 V and 400 °C at −375 V, with an estimated

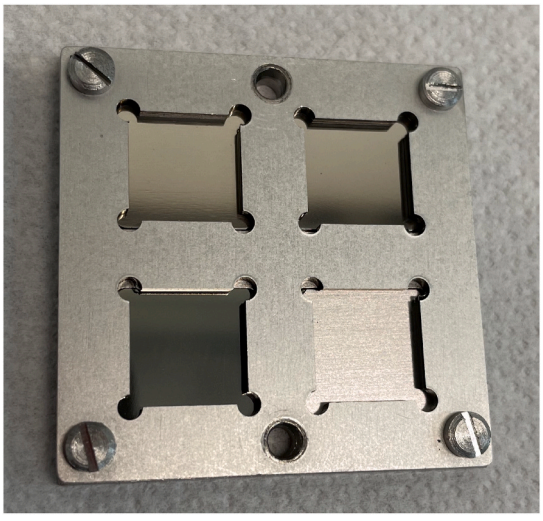

**Fig. 2.** Picture of the tiles (TW2 on the top left corner, ZW6 on the top right corner, HW6 on the bottom left corner, reference W on the bottom right corner) mounted in the sample holder before deuterium plasma irradiation in the linear device GyM.

thermal load of about 50 kW/m$^2$.

To study the damage caused by charged particles near the divertor, irradiation with protons was carried out in polished UHTC tiles [45,46]. The estimated dose delivered was 30–60 Gy (50–65 shots on the sample characterized by 6-30 × 10$^5$ p/shot and 0.3 Gy/min).

### 2.4. Thermal characterization

The thermal conductivity of the sample surfaces subjected to deuterium plasma at the maximum ion energies of 400 eV were characterized by the VertiSenseTM scanning thermal microscopy technique using an AFM probe with an embedded thermocouple (an AppNano SThM probe) that worked in thermal conductivity contrast mode. In this mode, the thermocouple of the probe was heated to a few degrees above the room temperature by positioning the AFM laser on the back of the cantilever closer to the tip base. In this way, the heat loss from the thermocouple to the sample is monitored as a change in the temperature (detecting a change less than 0.01 °C) generating a thermal conductivity map in conjunction with the topography [47]. The scanned area was chosen by optical microscope observation so that the border between the plasma-exposed area and the untreated area (covered by the sample holder mask) was approximately in the center. The areas of 50 μm × 50 μm were scanned for the UHTC samples and 100 μm × 100 μm for the tungsten samples, where it was difficult to identify the border separating the treated area from the untreated area.

Thermal diffusivity was measured using a laser flash analyser (Linseis LFA 1000, Germany). A thin graphite layer was sprayed onto both sides of the tiles before measurements to hinder any reflection of the laser beam or improve emissivity on the back side of the samples. Each measurement is an average of 3 tests, which were performed at several temperatures from room temperature to 1200 °C in Ar flux. The standard deviation of the average values of thermal diffusivity of the samples was 3 %. To evaluate the effect of exposure in relevant environments on the thermal properties of $MB_2$-WC materials, these measurements were performed on the irradiated tiles as well as the pristine polished surfaces and the reference tungsten samples. Since the reference tungsten samples were not polished, the thermal diffusivity was also measured on the as-machined $MB_2$-WC tiles to provide a consistent comparison.

## 3. Results and discussion

### 3.1. Densification behaviour

High-density samples (>97 %, see Table 2) were obtained despite a dwell time lower than that reported in literature [48,49]. TW2 samples showed the lowest onset temperature ($T_{ON}$) of 1010 °C. This temperature is quite low compared to other similar $TiB_2$-based materials [50], and is in agreement with the previous work [39]. However, the sintering phenomena start to slow down before the maximum temperature is reached, as indicated by the peak of the densification rate curve occurring well before the dwell step and the plateauing of the curve at 97 % before the start of dwell time (Fig. 1a). This sintering behaviour can be attributed to the presence of Co, which promotes liquid sintering mechanisms that require lower temperatures to be activated, but were not sufficient to complete densification [51]. ZW6 samples reached full densification quickly, while HW6 samples required a longer isothermal hold due to the refractory nature of $HfB_2$. In particular, $ZrB_2$-based material showed the highest densification rate value of 7.3 % min$^{-1}$ allowing full densification within a limited dwell time. It is worth noting that the observed $T_{ON}$ of 1400 °C is lower than those reported for $ZrB_2$ with other ceramic sintering aids ($Si_3N_4$, SiC, $Y_2O_3$, $Al_2O_3$, ZrN) [52–54]. A lower $T_{ON}$ was only obtained when using Ni as the sintering aid [55]. However, Ni prevented grain growth, which is desired to increase the thermal conductivity. For this reason, although the activation of densification mechanisms at low temperature and reaching the plateau took less than 15 min, the isothermal hold was extended to 30 min to ensure a

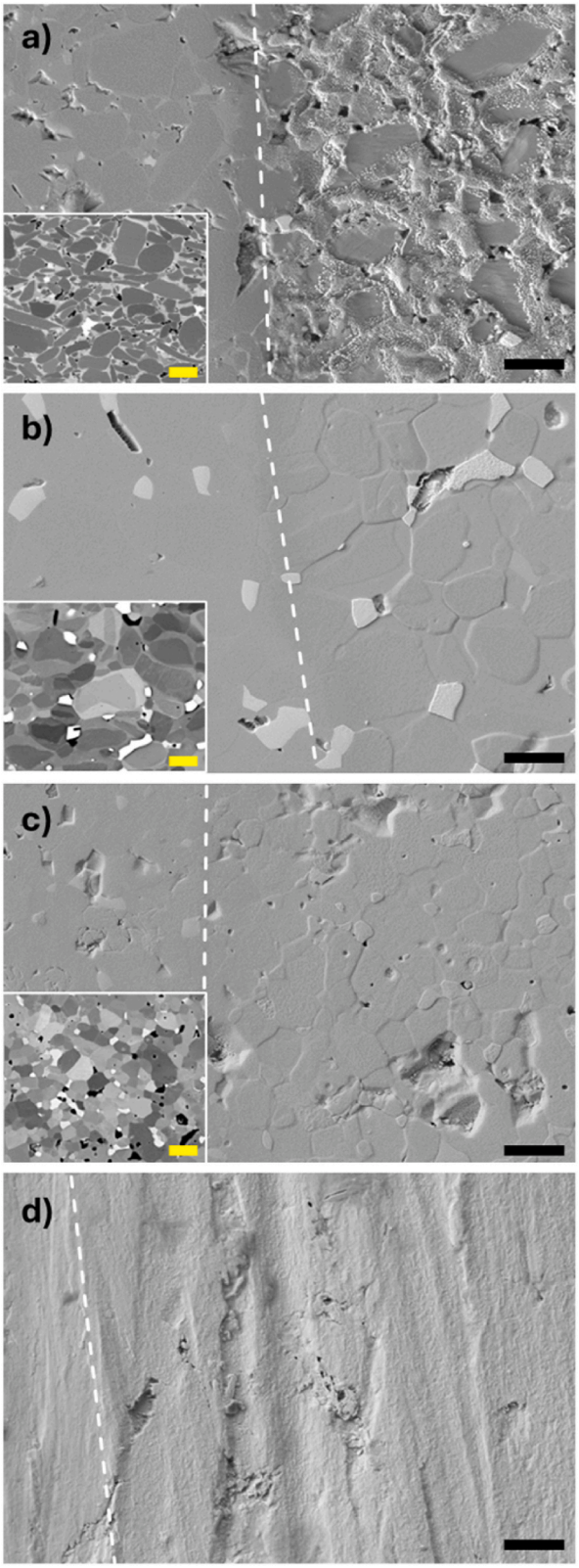


**Fig. 3.** SEM images of (a) TW2, (b) ZW6, (c) HW6 and (d) W tiles subjected to deuterium plasma irradiation at ion energies of 400 eV for 5 h. In all micrographs, the border between the untreated area (on the left side) and the plasma-exposed area (on the right side) is approximately in the center of the image. The insets show BSE images of untreated area. The length of all scale bars is 2 μm. A thin dashed line was placed indicatively among the two area.

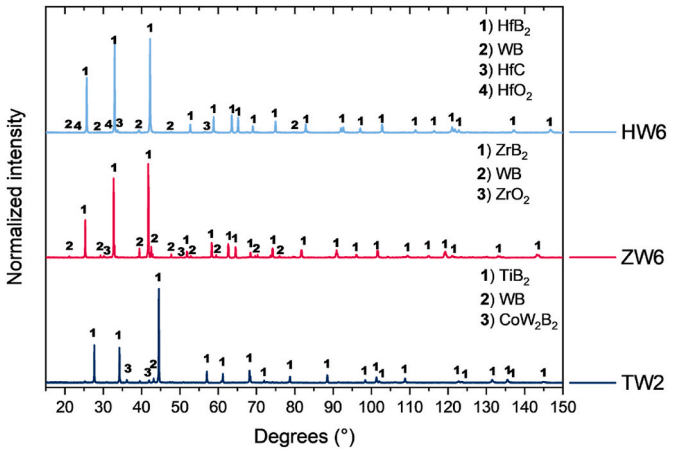


**Fig. 4.** XRD diffractograms from the materials TW2 (bottom diffractogram), ZW6 (centre diffractogram) and HW6 (top diffractogram).

coarse and homogeneous microstructure and to raise the thermal conductivity. Noteworthy, the manufacturing process of this work allowed to reduce the starting densification temperature ($T_{ON}$) compared to similar $ZrB_2$ materials [56] containing higher amount of starting WC (15 vol% instead of 4.1 vol%). Another reason for this lower sintering onset could be the high thickness of pellet (24–30 mm instead of 10 mm [57]), which allows earlier detection of shrinkage due to measurement sensitivity, even though the actual sintering temperature remains the same. Additionally, Co traces from milling with WC media reduce $T_{ON}$. The lower sinterability of the $HfB_2$-based material, indicated by the higher $T_{ON}$ of 1700 °C and lower densification rate (peak value of 3.2 % $min^{-1}$), was compensated by a longer isothermal hold. This requirement is due to the more refractory behaviour of $HfB_2$ compared to $ZrB_2$, which includes a higher melting point and lower transport rates [53,54,58].

### 3.2. Microstructure

SEM analysis confirmed low levels of residual porosity in TW2 and HW6 samples, with nearly pores-free ZW6 sample (Fig. 3). A core-shell structure (more pronounced in ZW6 sample) was observed in all samples, indicating the formation of solid solutions of diborides with tungsten. The core consists of $MB_2$, while the shell consists of (M, W)$B_2$ solid solution cores (M = Ti, Zr, or Hf). This result confirms the active role of WC in effectively promoting densification during hot-pressing and indicates that the starting diborides and tungsten are mutually soluble at high temperatures, as previously reported [56,59,60]. The WB phase

**Table 3**
Indexed phases in the XRD diffractograms of the analyzed samples.

| Sample | Main phase | Secondary phases |
|---|---|---|
| TW2 | Hexagonal $TiB_2$: *P6/mmm*(191), PDF # 65–1073, ρ: 4.497 g/cm$^3$ | - Orthorhombic WB: *Cmcm*(63), PDF # 06–0541, ρ: 15.72 g/cm$^3$<br>- Orthorhombic $CoW_2B_2$: *Immm*(71), PDF # 65–2530, ρ: 14.521 g/cm$^3$ |
| ZW6 | Hexagonal $ZrB_2$: *P6/mmm*(191), PDF #34–0423, ρ:6.104 g/cm$^3$ | - Tetragonal WB: *I4$_1$/amd*(141), PDF #35–0738, ρ:15.744 g/cm$^3$<br>- Cubic $ZrO_2$: Fm3m(225), PDF # 49–1642; ρ: 6.069 g/cm$^3$ |
| HW6 | Hexagonal $HfB_2$: *P6/mmm*(191), PDF # 38–1398, ρ: 11.178 g/cm3 | - Tetragonal WB: *I4$_1$/amd*(141), PDF #35–0738, ρ:15.744 g/cm$^3$<br>- Monoclinic $HfO_2$: P21/a(14), PDF # 34–0104, ρ: 10.10 g/cm$^3$<br>- Cubic HfC: Fm3m(225), PDF # 39–1491, ρ: 12.686 g/cm3 |

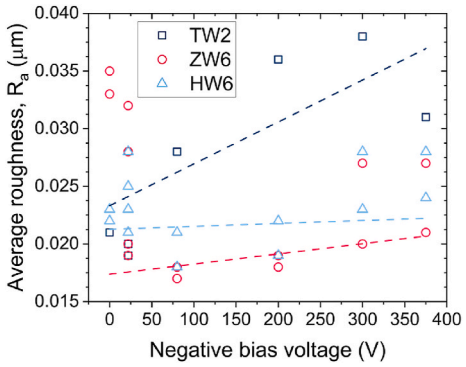


**Fig. 5.** $R_a$ values as a function of applied bias voltage for deuterium plasma irradiation.

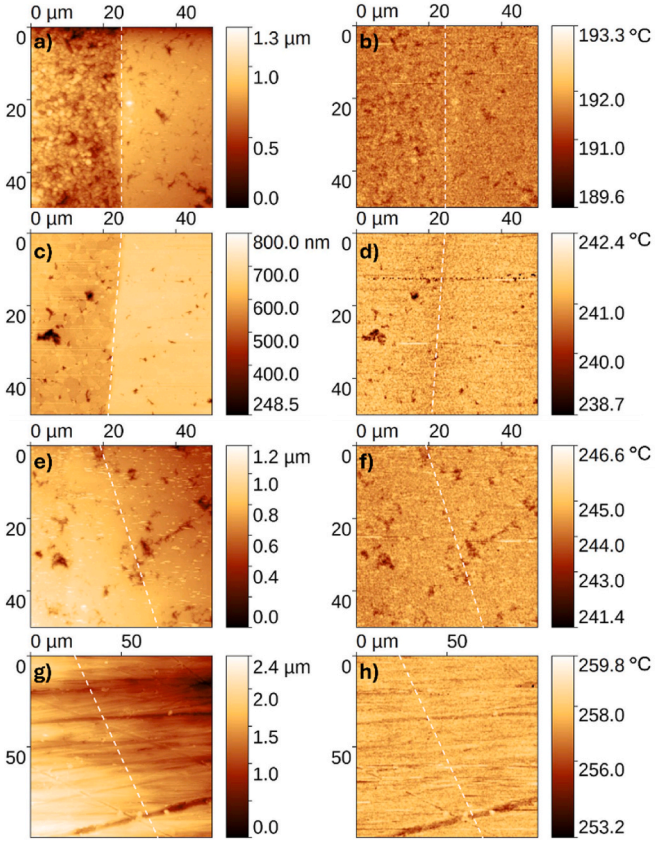


**Fig. 6.** Topography (left column) and temperature maps (right column) for (a, b) TW2, (c, d) ZW6, (e, f) HW6 and (g, h) W tiles irradiated with deuterium plasma at ion energies of 400 eV for 5 h. In all the images the plasma-exposed area is on the left side and the untreated area is on the right side. A thin dashed line was placed indicatively among the two area.

appeared as a lighter, homogeneously distributed phase. The ZW6 sample showed the presence of free carbon appearing as a dark elongated shape.

XRD patterns showed crystalline diborides as the main phase (Fig. 4). Various secondary and minor phases were detected in the UHTC samples (Table 3). In case of TW2 sample, the main phase was identified as hexagonal $TiB_2$, with orthorhombic WB and orthorhombic $CoW_2B_2$ as secondary phases. For ZW6 sample, the main phase was hexagonal $ZrB_2$. Due to the higher amount of staring WC in ZW6 material compared to TW2 (10 wt% instead of the expected 5.4 wt%), the WB peaks were more prominent forming a tetragonal lattice as seen in a similar material with

15 vol% of starting WC instead of 4.1 vol% [56] and other $ZrB_2$-based ceramics with WC [61,62]. ZW6 sample also showed traces of cubic $ZrO_2$. For HW6 sample the main phase was hexagonal $HfB_2$. A small amount of staring WC resulted in smaller peaks of tetragonal WB, similar to ZW6. The oxidic $HfO_2$ phase showed a monoclinic lattice. Unlike ZW6, which had dispersed free carbon (Fig. 3b), HW6 had carbon forming cubic HfC. The peak shift toward higher 2-theta angles suggests that HfC is a solid solution containing W atoms [56]. Notably, SEM analysis showed no microcracks in ZW6 or HW6 due to the presence of oxidic phases [48].

### 3.3. Surface roughness

While no microstructure changes were observed after proton irradiation, deuterium plasma exposure led to surface erosion and texture modifications (Fig. 3). A distinct change in surface topology around the grains is visible in the irradiated region. Despite this, $R_a$ values remained low (<0.04 μm, see Fig. 5), and the tendency for $R_a$ to increase with applied bias voltage was unclear, likely due to the manual polishing. Consistent with observations in similar UHTCs [63,64], the differences between the different borides are mainly due to varying levels of residual porosity. Specifically, the average $R_a$ values ranged from 0.019 μm for ZW6, to 0.022 μm for HW6 sample and 0.027 μm for TW2.

### 3.4. Thermal properties

Fig. 6 shows the topographic image (left column) and the temperature map (right column) for each UHTC sample, along with a reference tungsten material. The topography images show a distinct texture between the "treated" and "untreated" areas, with clear edges visible in all samples except for the tungsten material. Small temperature variations corresponding to surface features, such as holes or scratches, can be seen by comparing the images on the left and right. These local differences likely result from interactions between the probe tip and the sample surface features (slope, variation in contact area, or the surface water layer). The topography images (Fig. 6 left) underline the erosion effect caused by deuterium plasma, which led to noticeable height difference between treated and untreated areas. The steps in the horizontal profile are found to be 230 nm and 65 nm in samples TW2 and ZW6, respectively (see supplementary materials). However, no significant differences in the average temperature between treated and untreated areas were observed. A subtle contrast can be seen in the HW6 sample where the left side of the temperature image appears slightly darker (cooler), possibly indicating an increased thermal conductivity. However, this variation is gradual, not steep, and of a small magnitude (approximately 0.02 °C). The analysis was not sensitive enough to detect changes in thermal conductivity after plasma interaction, confirming that thermal properties were not significantly affected by plasma exposure.

Similarly, thermal diffusivity analysis showed no clear trend related to plasma exposure or surface roughness among the investigated materials (Fig. 7). This result is somewhat expected, given that the samples were coated with a graphite layer, and the laser flash diffusivity technique measures bulk properties. Deuterium irradiation caused surface damage with a penetration depth of about 100 nm, which represents only 0.01 % of the sample's total volume. As a result, such surface damage is unlikely to significantly affect the measured thermal diffusivity. The thermal diffusivity data were fitted with equation $D = a + b/T + c/T^2$ [65], yielding the following fitted parameters with $R^2 > 0.99$:

$$D_{TW2} = (11.37 \pm 0.10) + (980 \pm 135)/T + (447264 \pm 38401)/T^2 \quad (1)$$

$$D_{ZW6} = (14.35 \pm 0.10) + (39 \pm 121)/T + (332062 \pm 31274)/T^2 \quad (2)$$

$$D_{HW6} = (13.57 \pm 0.15) + (1748 \pm 206)/T + (488635 \pm 57492)/T^2 \quad (3)$$

$$D_{W} = (26.40 \pm 0.43) + (19041 \pm 606)/T - (1853939 \pm 167294)/T^2 \quad (4)$$

Thermal conductivities were not measured directly, but were calculated as a function of temperature from fitted thermal diffusivities, D (Eqs. (1)–(4)), and constant pressure-specific heat capacities, $c_p$, using the equation: $k = D \cdot \rho \cdot c_p$. The constant pressure-specific heat capacity was extrapolated by fitting the data from the NIST-JANAF tables and

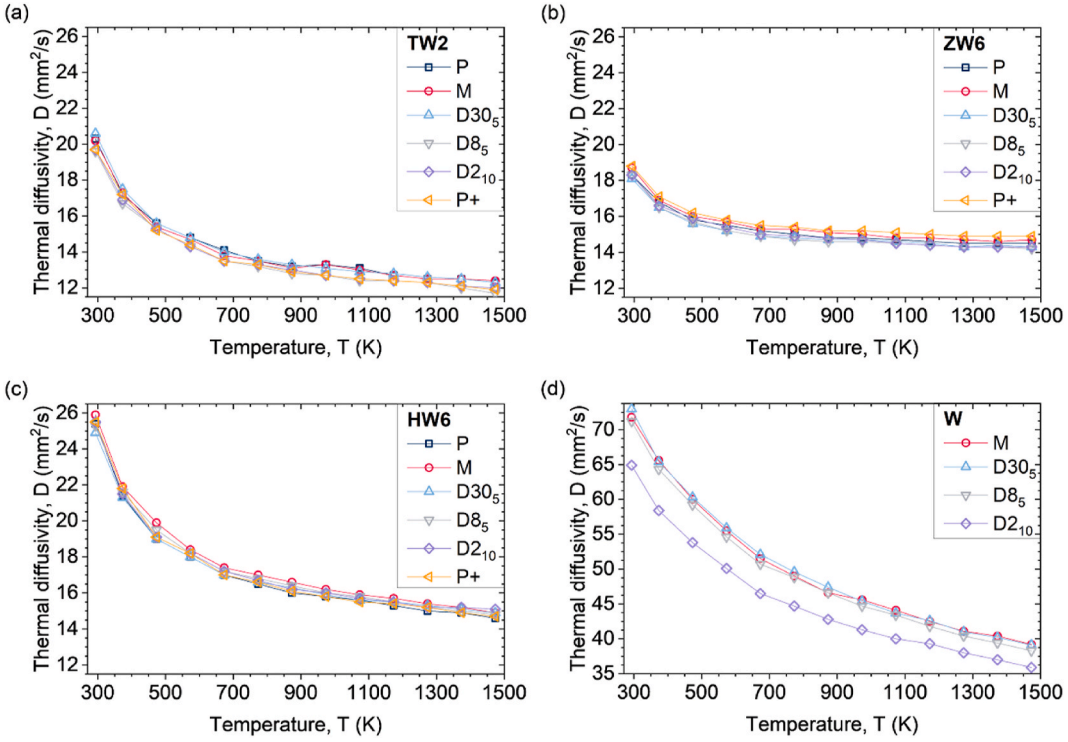


**Fig. 7.** Thermal diffusivity (D) as a function of temperature (T) for the as machined (M), polished (P), irradiated with deuterium plasma at −80 V for 5 h ($D8_5$), −22 V for 10 h ($D2_{10}$), and −300 V for 5 h ($D30_5$), and irradiated with protons (P+) tiles of (a) TW2, (b) ZW6, (c) HW6 and (d) W.

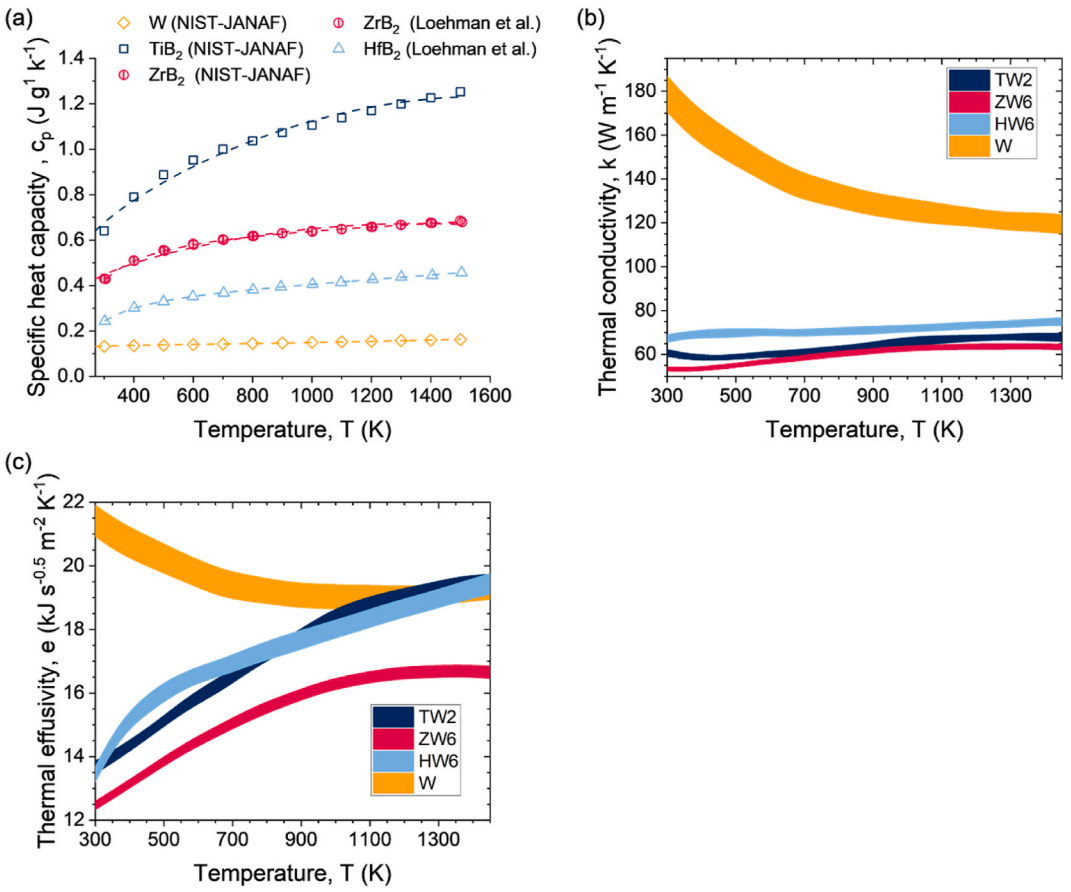


**Fig. 8.** (A) Specific heat capacity ($c_p$) as a function of temperature (T) taken from the literature and fitted with the typical $c_p = a+b{\cdot}T + c{\cdot}T^{-2}+d{\cdot}T^2$ relationship [27]. NIST-JANAF reference data for pure $TiB_2$ ($c_p$ = 0.46361 + 9.70484·10$^{-4}$·T - 4543.66731·T$^{-2}$ - 3.05291·10$^{-7}$·T$^2$), $ZrB_2$ ($c_p$ = 0.35486 + 4.73193·10$^{-4}$·T - 2977.70907·T$^{-2}$ - 1.75125·10$^{-7}$·T$^2$), W ($c_p$ = 0.1374 + 2.19278·10$^{-6}$·T - 499.23917·T$^{-2}$ + 1.01535·10$^{-8}$·T$^2$). Data reported by Loehman et al. [66] for pure $ZrB_2$ ($c_p$ = 0.56414 + 1.08089·10$^{-4}$·T - 15593.75217·T$^{-2}$ - 1.76558·10$^{-8}$·T$^2$), and $HfB_2$ ($c_p$ = 0.32802 + 8.43108·10$^{-5}$·T - 10014.47319·T$^{-2}$ + 2.84412·10$^{-9}$·T$^2$). (b) Calculated thermal conductivity (k) as a function of T. (c) Calculated thermal effusivity (e) as a function of T. The curves reported in Fig. 8b and c represent the interval of TW2 (blue curve), ZW6 (red curve), HW6 (light blue curve), and W (orange curve), calculated taking into account the thermal diffusivity measured on the different types of samples: as-machined (M), polished (P), irradiated with deuterium plasma at −80 V for 5 h (D85), −22 V for 10 h (D210), and −300 V for 5 h (D305), as well as samples irradiated with protons (P+). (For interpretation of the references to colour in this figure legend, the reader is referred to the Web version of this article.)

those reported by Loehman et al. [66], as shown in Fig. 8a. The effect of temperature on the sample density (ρ) was not taken into account and the values reported in Table 2 were kept constant. The calculated thermal conductivities are shown in Fig. 8b. Contrary to the reference tungsten material, the UHTCs showed an increase of thermal conductivity with the increasing temperature. This behavior, coupled with thermal conductivity values exceeding 50 W m$^{-1}$ K$^{-1}$, confirms the application potential of these UHTCs materials for PFMs. While the thermal property results of materials exposed in GyM are encouraging and suggest that $MB_2$-WC composites could be considered as potential PFMs, it is important to note that these findings are preliminary. The GyM facility can simulate the particle fluxes expected in the main chamber of tokamaks, but it cannot replicate the high thermal loads of the order of MW/m$^2$ that impact the first wall. These thermal loads are the primary drivers of changes in the thermo-mechanical properties of plasma-facing components (PFCs). Therefore, further testing under more representative thermal conditions is necessary to fully evaluate the suitability of $MB_2$-WC composites as PFMs. For the future development of these materials, the incorporation of carbon fibers reinforcement has the potential to enhance the thermal shock resistance and even thermal conductivity [67]. However, careful consideration must be given to the amount and arrangement of carbon fibers to balance the thermo-mechanical properties of the fiber-reinforced composites [68,69] and to manage deuterium retention, which can be affected by the presence of carbon fiber [20]. Finally, it is worth noting that even the thermal effusivity (calculated as $e = D^{0.5}{\cdot}\rho{\cdot}c_p$) of $MB_2$-WC ceramics increased with temperature, while the thermal effusivity of tungsten decreased (Fig. 8c). For TW2 and HW6 samples, the thermal effusivity approaches that of tungsten at approximately 930 ± 40 °C and 1100 ± 20 °C, respectively, and exceeds it by 1 % at 1200 °C. This result is significant because thermal effusivity is a key measure of a material thermal inertia and its ability to withstand thermal spikes, which are common in nuclear fusion reactors [20]. In fact, during transient phenomena, such as thermal spikes, heat flow is proportional to thermal effusivity rather than thermal conductivity, which is relevant only under steady state conditions [70,71].

## 4. Conclusion

No significant deterioration of the thermal properties of $MB_2$-WC ceramics (M = Ti, Zr, Hf) was observed after the deuterium plasma exposure or proton irradiation, making these materials promising candidates for fusion applications. The measured thermal diffusivity ranged from 20.0 ± 0.4 to 12.1 ± 0.3 mm$^2$ s$^{-1}$ for $TiB_2$-2(WC-6Co), from 18.4 ± 0.2 to 14.5 ± 0.2 mm$^2$ s$^{-1}$ for $ZrB_2$-6WC, from 25.4 ± 0.3 to 14.8 ± 0.2 mm$^2$ s$^{-1}$ for $HfB_2$-6WC, and from 70.2 ± 3.1 to 38.1 ± 1.3 mm$^2$ s$^{-1}$ for tungsten reference material, across the temperature range from room temperature to 1200 °C. The corresponding calculated thermal conductivities ranged from 61 ± 1 to 68 ± 2 W m$^{-1}$ K$^{-1}$, from 53 ± 1 to 63 ± 1 W m$^{-1}$ K$^{-1}$, from 67 ± 2 to 75 ± 2 W m$^{-1}$ K$^{-1}$, and from 180 ± 8 to

119 ± 4 W $m^{-1}$ $K^{-1}$ for $TiB_2$-2(WC-6Co), $ZrB_2$-6WC, $HfB_2$-6WC and W, respectively. A key finding that supports further testing and characterization of these UHTCs for use as plasma-facing materials is their thermal effusivity. The thermal effusivity ranged from 13.6 ± 0.2 to 19.4 ± 0.3 kJ $s^{-0.5}$ $m^{-2}$ $K^{-1}$ for $TiB_2$-2(WC-6Co), from 12.4 ± 0.1 to 16.6 ± 0.2 kJ $s^{-0.5}$ $m^{-2}$ $K^{-1}$ for $ZrB_2$-6WC, from 13.3 ± 0.2 to 19.5 ± 0.2 kJ $s^{-0.5}$ $m^{-2}$ $K^{-1}$ for $HfB_2$-6WC. In contrast, tungsten showed a decreasing trend in thermal effusivity from 21.5 ± 0.5 to 19.3 ± 0.3 kJ $s^{-0.5}$ $m^{-2}$ $K^{-1}$, making it more susceptible to thermal spikes of nuclear fusion reactors.

## CRediT authorship contribution statement

**Pietro Galizia:** Writing – review & editing, Writing – original draft, Visualization, Validation, Supervision, Resources, Project administration, Methodology, Investigation, Funding acquisition, Formal analysis, Data curation, Conceptualization. **Andrea Uccello:** Writing – review & editing, Validation, Supervision, Resources, Methodology, Conceptualization. **Francesco Ghezzi:** Writing – review & editing, Validation, Supervision, Resources, Methodology, Conceptualization. **Luca Labate:** Software, Resources, Project administration, Methodology. **Bruno Tiribilli:** Writing – review & editing, Resources, Methodology, Investigation, Data curation. **Ondrej Hanzel:** Writing – review & editing, Resources, Investigation, Data curation. **Martina Salvadori:** Software, Resources, Methodology. **Fernando Brandi:** Resources, Methodology. **Simone Failla:** Writing – review & editing, Resources. **Cesare Melandri:** Investigation. **Anna Cremona:** Resources. **Matteo Pedroni:** Resources. **Marco De Angeli:** Resources. **Enrico Perelli Cippo:** Writing – review & editing, Supervision. **Leonida Antonio Gizzi:** Resources, Methodology. **Peter Tatarko:** Writing – review & editing, Project administration, Funding acquisition. **Diletta Sciti:** Writing – review & editing, Project administration, Funding acquisition.

## Declaration of competing interest

The authors declare that they have no known competing financial interests or personal relationships that could have appeared to influence the work reported in this paper.

## Acknowledgments

The research leading to these results has received funding from the joint research agreement ENI-CNR on nuclear fusion energy (CUPB34I19003070007, CNR DFM.AD006.155 JRA ENI-CNR – CdR FUSIONE). P.T and O.H. acknowledge the support of the project APVV-21-0402 and JRP SAV TUBITAK project No. 720464. L.L., M.S., F.B. and L.A.G. acknowledge support from the following projects: CNR-funded Italian research network ELI-Italy (D.M. No. 631 08.08.2016); EU NextGeneration EU "Integrated Infrastructure Initiative in Photonic and Quantum Sciences", I-PHOQS (IR0000016, ID D2B8D520, and CUP B53C22001750006), and "EuPRAXIA Advanced Photon Sources", EuAPS (IR0000030 and CUP I93C21000160006). The authors are grateful to the JECS Trust for funding the visit of Pietro Galizia to Institute of Inorganic Chemistry of Slovak Academy of Sciences in Bratislava (Contract No. 2023375). P.G. and B.T. acknowledge the project *Change the Game: Playing to be Trained for the Challenges of a Sustainable Society*, funded by progettidiricerca@CNR, which provided the opportunity, during a meeting on developing serious games with LEGO®, for BT to present the LEGO® AFM. This inspired the design of the thermal conductivity experiments using AFM, which were ultimately conducted by BT (playing) with a professional instrument.

## Appendix A. Supplementary data

Supplementary data to this article can be found online at https://doi.org/10.1016/j.oceram.2024.100696.

## References

[1] W.G. Fahrenholtz, G.E. Hilmas, I.G. Talmy, J.A. Zaykoski, Refractory diborides of zirconium and hafnium, J. Am. Ceram. Soc. 90 (2007) 1347–1364, https://doi.org/10.1111/j.1551-2916.2007.01583.x.
[2] W.G. Fahrenholtz, G.E. Hilmas, Ultra-high temperature ceramics: materials for extreme environments, Scripta Mater. 129 (2017) 94–99, https://doi.org/10.1016/j.scriptamat.2016.10.018.
[3] B.R. Golla, A. Mukhopadhyay, B. Basu, S.K. Thimmappa, Review on ultra-high temperature boride ceramics, Prog. Mater. Sci. 111 (2020) 100651, https://doi.org/10.1016/j.pmatsci.2020.100651.
[4] B.C. Wyatt, S.K. Nemani, G.E. Hilmas, E.J. Opila, B. Anasori, Ultra-high temperature ceramics for extreme environments, Nat. Rev. Mater. (2023) 1–17, https://doi.org/10.1038/s41578-023-00619-0.
[5] N.P. Padture, Advanced structural ceramics in aerospace propulsion, Nat. Mater. 15 (2016) 804–809, https://doi.org/10.1038/nmat4687.
[6] J. Binner, M. Porter, B. Baker, J. Zou, V. Venkatachalam, V.R. Diaz, A. D'Angio, P. Ramanujam, T. Zhang, T.S.R.C. Murthy, Selection, processing, properties and applications of ultra-high temperature ceramic matrix composites, UHTCMCs–a review, Int. Mater. Rev. 65 (2020) 389–444, https://doi.org/10.1080/09506608.2019.1652006.
[7] P. Galizia, D. Sciti, N. Jain, Insight into microstructure and flexural strength of ultra-high temperature ceramics enriched SICARBON$^{TM}$ composite, Mater. Des. (2021) 109888, https://doi.org/10.1016/j.matdes.2021.109888.
[8] S.R.C.M. Tammana, M. Duan, J. Zou, J. Wade, V. Venkatachalam, B. Baker, S. Nayebossadri, J. Binner, Ablation behaviour of Cf–ZrC-SiC with and without rare earth metal oxide dopants, Open Ceramics 10 (2022) 100270, https://doi.org/10.1016/J.OCERAM.2022.100270.
[9] P. Galizia, D. Sciti, Disclosing residual thermal stresses in UHT fibre-reinforced ceramic composites and their effect on mechanical behaviour and damage evolution, Compos. B Eng. 248 (2023) 110369, https://doi.org/10.1016/J.COMPOSITESB.2022.110369.
[10] D. Sciti, A. Vinci, L. Zoli, P. Galizia, S. Failla, S. Mungiguerra, G.D.D. Martino, A. Cecere, R. Savino, Propulsion tests on ultra-high-temperature ceramic matrix composites for reusable rocket nozzles, Journal of Advanced Ceramics 12 (2023) 1345–1360, https://doi.org/10.26599/JAC.2023.9220759.
[11] B.A. Morris, S.J. Povolny, G.D. Seidel, C. Tallon, Effects of oxidation on the effective thermomechanical properties of porous ultra-high temperature ceramics in compression via computational micromechanics and MPM, Open Ceramics 15 (2023) 100382, https://doi.org/10.1016/j.oceram.2023.100382.
[12] L. Backman, J. Gild, M. Qin, J. Luo, E.J. Opila, Composition dependence of oxidation resistance in high entropy ultra-high temperature ceramics, Open Ceramics 18 (2024) 100563, https://doi.org/10.1016/j.oceram.2024.100563.
[13] D.M. Trucchi, A. Bellucci, M. Girolami, P. Calvani, E. Cappelli, S. Orlando, R. Polini, L. Silvestroni, D. Sciti, A. Kribus, Solar Thermionic-Thermoelectric generator (ST2G): concept, materials engineering, and prototype demonstration, Adv. Energy Mater. 8 (2018) 1802310, https://doi.org/10.1002/aenm.201802310.
[14] L.M. Garrison, G.L. Kulcinski, G. Hilmas, W. Fahrenholtz, H.M. Meyer, The response of ZrB2 to simulated plasma-facing material conditions of He irradiation at high temperature, J. Nucl. Mater. 507 (2018) 112–125, https://doi.org/10.1016/j.jnucmat.2018.04.016.
[15] A. Bhattacharya, C.M. Parish, T. Koyanagi, C.M. Petrie, D. King, G. Hilmas, W. G. Fahrenholtz, S.J. Zinkle, Y. Katoh, Nano-scale microstructure damage by neutron irradiations in a novel Boron-11 enriched TiB2 ultra-high temperature ceramic, Acta Mater. 165 (2019) 26–39, https://doi.org/10.1016/j.actamat.2018.11.030.
[16] T. Koyanagi, Y. Katoh, C. Ang, D. King, G.E. Hilmas, W.G. Fahrenholtz, Response of isotopically tailored titanium diboride to neutron irradiation, J. Am. Ceram. Soc. 102 (2019) 85–89, https://doi.org/10.1111/jace.16036.
[17] W. Bao, S. Robertson, J.-W. Zhao, J.-X. Liu, H. Wu, G.-J. Zhang, F. Xu, Structural integrity and damage of ZrB2 ceramics after 4 MeV Au ions irradiation, J. Mater. Sci. Technol. 72 (2021) 223–230, https://doi.org/10.1016/j.jmst.2020.09.019.
[18] L. Nuckols, C.M. Parish, M.J. Baldwin, H.M. Meyer, D. Nishijima, M.I. Patino, J. Rapp, Observation of tantalum deposition and growth on TiB2 and ZrB2 from PISCES-RF deuterium and helium plasma exposures, Nuclear Materials and Energy 39 (2024) 101641, https://doi.org/10.1016/j.nme.2024.101641.
[19] M.M. Nasseri, Comparison of HfB2 and ZrB2 behaviors for using in nuclear industry, Ann. Nucl. Energy 114 (2018) 603–606, https://doi.org/10.1016/j.anucene.2017.12.060.
[20] J. Linke, J. Du, T. Loewenhoff, G. Pintsuk, B. Spilker, I. Steudel, M. Wirtz, Challenges for plasma-facing components in nuclear fusion, Matter Radiat. Extremes 4 (2019) 056201, https://doi.org/10.1063/1.5090100.
[21] E.E. Bloom, S.J. Zinkle, F.W. Wiffen, Materials to deliver the promise of fusion power – progress and challenges, J. Nucl. Mater. 329–333 (2004) 12–19, https://doi.org/10.1016/j.jnucmat.2004.04.141.
[22] C. Yin, D. Terentyev, T. Zhang, S. Nogami, S. Antusch, C.-C. Chang, R.H. Petrov, T. Pardoen, Ductile to brittle transition temperature of advanced tungsten alloys for nuclear fusion applications deduced by miniaturized three-point bending tests, Int. J. Refract. Metals Hard Mater. 95 (2021) 105464, https://doi.org/10.1016/j.ijrmhm.2020.105464.
[23] H. Zhang, X. Zhang, Y. Li, P. Wang, L. Qiao, Effects of deuterium plasma exposure and helium ions irradiation on nanoindentation hardness of tungsten, Nuclear Materials and Energy 40 (2024) 101722, https://doi.org/10.1016/j.nme.2024.101722.

[24] L. Gao, M. Wilde, A. Manhard, U. von Toussaint, W. Jacob, Hydrogen atom-ion synergy in surface lattice modification at sub-threshold energy, Acta Mater. 201 (2020) 55–62, https://doi.org/10.1016/j.actamat.2020.09.065.

[25] M. Athanasakis, E. Ivanov, E. del Rio, S.A. Humphry-Baker, A high temperature W2B–W composite for fusion reactor shielding, J. Nucl. Mater. 532 (2020) 152062, https://doi.org/10.1016/j.jnucmat.2020.152062.

[26] G.J.K. Harrington, G.E. Hilmas, Thermal conductivity of ZrB2 and HfB2, in: Ultra-High Temperature Ceramics, John Wiley & Sons, Ltd, 2014, pp. 197–235, https://doi.org/10.1002/9781118700853.ch9.

[27] J.W. Zimmermann, G.E. Hilmas, W.G. Fahrenholtz, R.B. Dinwiddie, W.D. Porter, H. Wang, Thermophysical properties of ZrB2 and ZrB2–SiC ceramics, J. Am. Ceram. Soc. 91 (2008) 1405–1411, https://doi.org/10.1111/J.1551-2916.2008.02268.X.

[28] M. Mallik, A.J. Kailath, K.K. Ray, R. Mitra, Electrical and thermophysical properties of ZrB2 and HfB2 based composites, J. Eur. Ceram. Soc. 32 (2012) 2545–2555, https://doi.org/10.1016/j.jeurceramsoc.2012.02.013.

[29] J.F. Justin, A. Jankowiak, Ultra high temperature ceramics : densification, properties and thermal stability, Aerospace Lab (2011) 1–11.

[30] L. Zhang, D.A. Pejaković, J. Marschall, M. Gasch, Thermal and electrical transport properties of spark plasma-sintered HfB2 and ZrB2 ceramics, J. Am. Ceram. Soc. 94 (2011) 2562–2570, https://doi.org/10.1111/j.1551-2916.2011.04411.x.

[31] H. Zhang, X. Zhang, L. Qiao, P. Wang, Deuterium retention in tungsten and tungsten alloys exposed to pure and impurities seeding deuterium plasma, Nuclear Materials and Energy 25 (2020) 100822, https://doi.org/10.1016/j.nme.2020.100822.

[32] M. Shimada, R. Pitts, A. Loarte, D.J. Campbell, M. Sugihara, V. Mukhovatov, A. Kukushkin, V. Chuyanov, ITER research plan of plasma–wall interaction, J. Nucl. Mater. 390–391 (2009) 282–285, https://doi.org/10.1016/j.jnucmat.2009.01.113.

[33] O. Hanzel, Z. Lenčéš, Y.-W. Kim, J. Fedor, P. Šajgalík, Highly electrically and thermally conductive silicon carbide-graphene composites with yttria and scandia additives, J. Eur. Ceram. Soc. 40 (2020) 241–250, https://doi.org/10.1016/j.jeurceramsoc.2019.10.001.

[34] M. Shojaie-bahaabad, M. Bozorg, M. Najafizadeh, P. Cavaliere, Ultra high temperature ceramic coatings in thermal protection systems (TPS), Ceram. Int. 50 (2024) 9937–9951, https://doi.org/10.1016/j.ceramint.2023.12.372.

[35] P. Galizia, S. Failla, L. Zoli, D. Sciti, Tough salami-inspired Cf/ZrB2 UHTCMCs produced by electrophoretic deposition, J. Eur. Ceram. Soc. 38 (2018) 403–409, https://doi.org/10.1016/j.jeurceramsoc.2017.09.047.

[36] P. Galizia, D. Sciti, F. Saraga, L. Zoli, Off-axis damage tolerance of fiber-reinforced composites for aerospace systems, J. Eur. Ceram. Soc. 40 (2020) 2691–2698, https://doi.org/10.1016/j.jeurceramsoc.2019.12.038.

[37] C. Zhang, P. Hu, L. Xun, Y. Zhou, J. Han, X. Zhang, A universal strategy towards the fabrication of ultra-high temperature ceramic matrix composites with outstanding mechanical properties and ablation resistance, Compos. B Eng. 280 (2024) 111485, https://doi.org/10.1016/j.compositesb.2024.111485.

[38] A.R. Mishra, V. Singh, M. Patel, R. Mitra, Effect of increased intra-bundle spacing on mechanical behaviour of Cf- ZrB2–SiC ultra-high temperature ceramic matrix composites produced by slurry infiltration and hot pressing, Open Ceramics 19 (2024) 100656, https://doi.org/10.1016/j.oceram.2024.100656.

[39] S. Failla, C. Melandri, L. Zoli, G. Zucca, D. Sciti, Hard and easy sinterable B4C-TiB2-based composites doped with WC, J. Eur. Ceram. Soc. 38 (2018) 3089–3095, https://doi.org/10.1016/J.JEURCERAMSOC.2018.02.041.

[40] D. Sciti, S. Failla, S. Turan, U. Savaci, P. Galizia, Properties and ballistic tests of strong B4C-TiB2 composites densified by gas pressure sintering, J. Eur. Ceram. Soc. 43 (2023) 1334–1342, https://doi.org/10.1016/j.jeurceramsoc.2022.11.066.

[41] P. Tatarko, S. Grasso, A. Kovalčíková, D. Medveď, I. Dlouhý, M.J. Reece, Highly textured and strongly anisotropic TiB2 ceramics prepared using magnetic field alignment (9T), J. Eur. Ceram. Soc. 40 (2020) 1111–1118, https://doi.org/10.1016/j.jeurceramsoc.2019.11.006.

[42] S. Chao, J. Goldsmith, D. Banerjee, Titanium diboride composite with improved sintering characteristics, Int. J. Refract. Metals Hard Mater. 49 (2015) 314–319, https://doi.org/10.1016/j.ijrmhm.2014.06.008.

[43] J. Song, C. Huang, B. Zou, H. Liu, L. Liu, J. Wang, Effects of sintering additives on microstructure and mechanical properties of TiB2–WC ceramic–metal composite tool materials, Int. J. Refract. Metals Hard Mater. 30 (2012) 91–95, https://doi.org/10.1016/j.ijrmhm.2011.07.008.

[44] A. Uccello, W. Bin, A. Bruschi, F. Causa, A. Cremona, M. De Angeli, D. Farina, G. Gatto, G. Gervasini, F. Ghezzi, G. Gittini, G. Granucci, G. Grosso, L. Laguardia, M. Lontano, V. Mellera, D. Minelli, A. Nardone, M. Pedroni, F. Ripamonti, N. Rispoli, E. Vassallo, D. Ricci, Linear plasma device GyM for plasma-material interaction studies, Front. Physiol. 11 (2023), https://doi.org/10.3389/fphy.2023.1108175.

[45] F. Brandi, L. Labate, D. Palla, S. Kumar, L. Fulgentini, P. Koester, F. Baffigi, M. Chiari, D. Panetta, L.A. Gizzi, A few MeV laser-plasma accelerated proton beam in air collimated using compact permanent quadrupole magnets, Appl. Sci. 11 (2021) 6358, https://doi.org/10.3390/app11146358.

[46] M. Salvadori, F. Brandi, L. Labate, F. Baffigi, L. Fulgentini, P. Galizia, P. Koester, D. Palla, D. Sciti, L.A. Gizzi, Quantitative elemental analysis of a specimen in air via external beam laser-driven particle-induced x-ray emission with a compact proton source, Phys. Rev. Appl. 21 (2024) 064020, https://doi.org/10.1103/PhysRevApplied.21.064020.

[47] VertiSense Thermal Microscopy, AppNano (n.d.). https://www.appnano.com/vertisense-thermal-microscopy (accessed May 28, 2024).

[48] D. Sciti, F. Monteverde, S. Guicciardi, G. Pezzotti, A. Bellosi, Microstructure and mechanical properties of ZrB2–MoSi2 ceramic composites produced by different sintering techniques, Materials Science and Engineering: A. 434 (2006) 303–309, https://doi.org/10.1016/j.msea.2006.06.112.

[49] A. Gubernat, Ł. Zych, K. Kornaus, D. Zientara, S. Komarek, K. Stan-Głowińska, P. Klimczyk, M. Podsiadło, J. Dusza, J. Lis, Z. Pędzich, The influence of sintering additives on densification and phase composition of ZrB2 – HfB2 composite, J. Eur. Ceram. Soc. 44 (2024) 116685, https://doi.org/10.1016/j.jeurceramsoc.2024.116685.

[50] S. Qiu, J. Zou, J. Liu, Y. Zhou, W. Ji, F. Zhang, W. Wang, Z. Fu, B4C–(Ti0.9Cr0.1)B2 composites with excellent specific hardness and enhanced toughness, J. Am. Ceram. Soc. 106 (2023) 4013–4022, https://doi.org/10.1111/jace.19078.

[51] S. Mashayekh, H.R. Baharvandi, Effects of WC contamination on the densification of spark plasma sintered monolithic HfB2, Open Ceramics 16 (2023) 100461, https://doi.org/10.1016/j.oceram.2023.100461.

[52] F. Monteverde, S. Guicciardi, A. Bellosi, Advances in microstructure and mechanical properties of zirconium diboride based ceramics, Mater. Sci. Eng. A 346 (2003) 310–319, https://doi.org/10.1016/S0921-5093(02)00520-8.

[53] F. Monteverde, A. Bellosi, Efficacy of HfN as sintering aid in the manufacture of ultrahigh-temperature metal diborides-matrix ceramics, J. Mater. Res. 19 (2004) 3576–3585, https://doi.org/10.1557/JMR.2004.0460.

[54] F. Monteverde, A. Bellosi, Development and characterization of metal-diboride-based composites toughened with ultra-fine SiC particulates, Solid State Sci. 7 (2005) 622–630, https://doi.org/10.1016/j.solidstatesciences.2005.02.007.

[55] F. Monteverde, A. Bellosi, S. Guicciardi, Processing and Properties of Zirconium Diboride-Based Composites, (n.d.).

[56] F. Monteverde, L. Silvestroni, Combined effects of WC and SiC on densification and thermo-mechanical stability of ZrB2 ceramics, Mater. Des. 109 (2016) 396–407, https://doi.org/10.1016/j.matdes.2016.06.114.

[57] L. Silvestroni, Laboratory Notebook: Combined Effects of WC and SiC on Densification and Thermo-Mechanical Stability of ZrB2 Ceramics., n.d.

[58] F. Monteverde, A. Bellosi, L. Scatteia, Processing and properties of ultra-high temperature ceramics for space applications, Mater. Sci. Eng. 485 (2008) 415–421, https://doi.org/10.1016/j.msea.2007.08.054.

[59] C. Schmalzried, R. Telle, B. Freitag, W. Mader, Solid state reactions in transition metal diboride-based materials, Int. J. Mater. Res. 92 (2001) 1197–1202, https://doi.org/10.3139/ijmr-2001-0221.

[60] R. Xu, H. Chen, J. Zhang, G. Xiao, M. Yi, Z. Chen, X. Meng, C. Xu, Preparation of WC@graphene reinforced titanium diboride-based composite ceramic materials fabricated via SPS, International Journal of Applied Ceramic Technology n/a (n.d.). https://doi.org/10.1111/ijac.14832.

[61] J. Zou, S.-K. Sun, G.-J. Zhang, Y.-M. Kan, P.-L. Wang, T. Ohji, Chemical reactions, anisotropic grain growth and sintering mechanisms of self-reinforced ZrB2–SiC doped with WC, J. Am. Ceram. Soc. 94 (2011) 1575–1583, https://doi.org/10.1111/j.1551-2916.2010.04278.x.

[62] H.-B. Ma, Z.-Y. Man, J.-X. Liu, F.-F. Xu, G.-J. Zhang, Microstructures, solid solution formation and high-temperature mechanical properties of ZrB2 ceramics doped with 5 vol.% WC, Mater. Des. 81 (2015) 133–140, https://doi.org/10.1016/j.matdes.2015.05.038.

[63] E. Sani, L. Mercatelli, M. Meucci, A. Balbo, L. Silvestroni, D. Sciti, Compositional dependence of optical properties of zirconium, hafnium and tantalum carbides for solar absorber applications, Sol. Energy 131 (2016) 199–207, https://doi.org/10.1016/j.solener.2016.02.045.

[64] E. Sani, L. Mercatelli, M. Meucci, L. Silvestroni, A. Balbo, D. Sciti, Process and composition dependence of optical properties of zirconium, hafnium and tantalum borides for solar receiver applications, Sol. Energy Mater. Sol. Cell. 155 (2016) 368–377, https://doi.org/10.1016/j.solmat.2016.06.028.

[65] M. Pertermann, A.G. Whittington, A.M. Hofmeister, F.J. Spera, J. Zayak, Transport properties of low-sanidine single-crystals, glasses and melts at high temperature, Contrib. Mineral. Petrol. 155 (2008) 689–702, https://doi.org/10.1007/s00410-007-0265-x.

[66] R. Loehman, E. Corral, H.P. Dumm, P. Kotula, R. Tandon, Ultra High Temperature Ceramics for Hypersonic Vehicle Applications, Sandia National Laboratories (SNL), Albuquerque, NM, and Livermore, CA (United States), 2006, https://doi.org/10.2172/887260.

[67] F. Wang, C. Zhang, X. Geng, Q. Gao, L. Xun, W. Wang, X. Zhang, P. Hu, Fabrication and multiscale heat transfer modeling of high thermal conductivity Cf/HfB2-SiC composites, Compos. Struct. 351 (2024) 118551, https://doi.org/10.1016/j.compstruct.2024.118551.

[68] P. Galizia, L. Zoli, D. Sciti, Impact of residual stress on thermal damage accumulation, and Young's modulus of fiber-reinforced ultra-high temperature ceramics, Mater. Des. 160 (2018) 803–809, https://doi.org/10.1016/J.MATDES.2018.10.019.

[69] P. Galizia, S. Failla, C. Melandri, D. Sciti, Local indentation response of carbon fibers embedded in a harsh environment: the sintered ultra-high temperature ceramic matrix, J. Eur. Ceram. Soc. 44 (2024) 5347–5357, https://doi.org/10.1016/j.jeurceramsoc.2023.12.025.

[70] E. Marín, The role of thermal properties in periodic time-varying phenomena, Eur. J. Phys. 28 (2007) 429, https://doi.org/10.1088/0143-0807/28/3/005.

[71] A. Jain, The role of thermal effusivity in heat exchange between finite-sized bodies, Int. J. Heat Mass Tran. 202 (2023) 123721, https://doi.org/10.1016/j.ijheatmasstransfer.2022.123721.